Photogenerated metasurfaces at terahertz frequencies induced by a continuous-wave low pump

Eduardo Alvear-Cabezón, Rafik Smaali, Emmanuel Centeno, F. Gonzalez-Posada, Thierry Taliercio

Photogenerated metasurfaces at terahertz frequencies induced by a continuous-wave low pump

Eduardo Alvear-Cabezón,* Rafik Smaali, and Emmanuel Centeno
Université Clermont Auvergne, CNRS, SIGMA Clermont, Institut Pascal, F-63000 Clermont-Ferrand, France

Fernando Gonzalez-Posada and Thierry Taliercio
Université Montpellier, CNRS, IES, UMR-5214, F-34090 Montpellier, France

(Received 2 February 2018; revised manuscript received 28 June 2018; published 27 July 2018)

Active metasurfaces have attracted a great deal of attention due to the unlimited ways of controlling electromagnetic radiation. In this work, we theoretically study the THz electromagnetic properties of photogenerated metasurfaces in an InAs slab. We use a spatially modulated optical pump to modify the permittivity. Those modifications are calculated by solving the ambipolar rate equation for the photocarriers. This work reveals the crucial impact of the photocarrier diffusion for realizing optimal metasurfaces for the control of THz radiation. We demonstrate that InAs is a promising semiconductor that could be used to manufacture fast and efficient on-chip THz components. We also demonstrate that low pump fluence in the continuous regime of only tens of $W\,cm^{-2}$ is sufficient to modulate the absorption of the THz waves up to 67% over a broad frequency range from 1 to 3 THz.

DOI: 10.1103/PhysRevB.98.035305

I. INTRODUCTION

The terahertz (THz) frequency is a part of the electromagnetic spectrum from 0.3 to 10 THz. Since the advent of efficient THz sources [1], a lot of efforts have been made toward realizing photonic components able to control THz radiation, which are crucial for several application domains, such as security [2], medical imaging [3], and wireless networks [4]. Among the different approaches, metasurfaces offer in particular a versatile platform for manipulating the phase, the polarization, or the intensity of electromagnetic waves [5–11]. Metasurfaces are composed of an array of metallic and/or dielectric resonators settled with a subwavelength period on a surface. The dynamical control of their electromagnetic properties has been explored by tuning their resonances with external stimuli, such as electrical, thermal, or mechanical actuators [12,13]. However, these approaches offer limited spectral and modulation actuations since the spectral shift for the resonances is accompanied by a decreasing efficiency. So far, all-optical modulators that have been realized use in particular Mie or plasmonic resonators [14–16]. A more attractive approach concerns photogenerated metasurfaces that yield fully reconfigurable devices operating over a wide range of frequencies [17,18]. In this approach, the permittivity of a semiconductor is locally modified by applying an optical excitation which is often a near infrared (IR) laser pump. The optical management of the permittivity is attributed to the shift of the plasma frequency in the THz range that depends on the photocarrier density. Photogenerated patterns of controlled size, shape, and spacing have for example been demonstrated with a spatially varied IR pump [19,20]. Ideally, these photogenerated patterns can be properly designed to achieve an optimal modulation of the THz signals [21]. The major issue that prevents the realization of on-chip integrated photogenerated components is the high pump power required to achieve a significant modulation of the THz signals. Although silicon is a material widely used for on-chip photonics, its indirect band gap prevents efficient photogeneration [22,23]. In the research of direct band gap semiconductors, photogenerated surfaces made of gallium arsenide (GaAs) have been realized with pump power attaining hundreds of kW/cm^2 [24,25]. However, these high fluences reached with pulsed lasers are incompatible with integrated on-chip sources that deliver low intensity in the continuous wave (CW) regime.

The choice of semiconductors capable of efficient photogeneration is thus crucial for the development of THz modulators operating at low pump power. Indium arsenide (InAs) is a promising candidate since it presents a reduced energy band gap $E_g^{\mathrm{InAs}} = 0.354$ eV at room temperature, which is about five times smaller than that of GaAs $E_g^{\mathrm{GaAs}} = 1.43$ eV. This leads to the enhancement of the IR absorption and consequently it increases the photocarrier density into InAs. The gain in terms of photocarrier density, denoted N, can be estimated by neglecting the diffusion of the carriers:

$$N = \frac{2}{hc}\tau_r \,\mathrm{Im}(\epsilon_{\mathrm{IR}})\Phi_0 \tag{1}$$

where h is the Planck constant, c the celerity of light, Φ_0 the pump fluence, ϵ_{IR} the relative permittivity of the semiconductor at pump wavelength (λ_{IR}), and τ_r the recombination time for the photocarriers. We consider here a 100% quantum efficiency by assuming that a photon generates an electron-hole pair. At $\lambda_{\mathrm{IR}} = 815$ nm, the respective recombination times and imaginary permittivities of GaAs and InAs are $\tau_r^{\mathrm{GaAs}} = 10$ ns and $\tau_r^{\mathrm{InAs}} = 100$ ns, $\mathrm{Im}(\epsilon_{\mathrm{IR}}^{GaAs}) = 0.6$ and $\mathrm{Im}(\epsilon_{\mathrm{IR}}^{\mathrm{InAs}}) = 3.3$ [26]. These parameters lead to a carrier density ratio $N^{\mathrm{InAs}}/N^{\mathrm{GaAs}} = 55$. Consequently, an equal carrier density

*eduardo_antonio.alvear_cabezon@etu.uca.fr

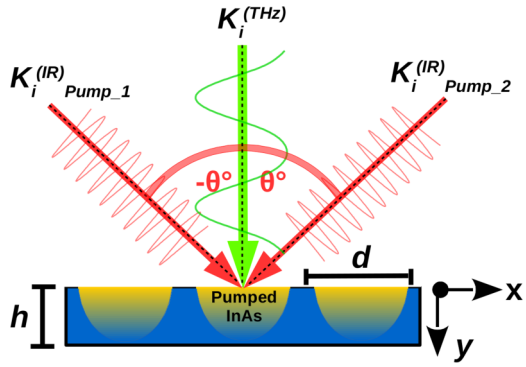

FIG. 1. Schematic of the interference pattern produced by two IR tilted plane waves with incident angles $\pm\theta$. The pumped InAs slab of thickness h and periodicity d is illuminated by a THz plane wave in normal incidence.

for InAs and GaAs requires a pump fluence 55 times lower for InAs than for GaAs. Nonetheless this result must be pondered by other crucial optical and electronic parameters such as the penetration distance L_p of the pump into the semiconductors and the ambipolar diffusion length L_a of the photocarriers. The high InAs absorption coefficient is indeed accompanied by a short penetration distance for the pump of about 147 nm compared to 810 nm for GaAs. This means that the active thickness of InAs, where more than 99% of the carriers are photogenerated, reaches only 1 μm (corresponding approximately to $10L_p$) against about 8 μm for GaAs. On the other hand, the ambipolar diffusion length that commands the diffusion of the photocarriers is 15.32 μm for InAs against 2 μm for GaAs [27]. Finally, for this specific experimental configuration ($\lambda_{\mathrm{IR}} = 815$ nm), even though the carriers are photogenerated in the first few hundreds of nm of the InAs layer, they diffuse seven times far away than into a GaAs layer. Finally, the photogenerated carrier distribution is dominated by the diffusion process for InAs and by the absorption process for GaAs. These physical features lead us to explore the potential of photogenerated metasurfaces based on InAs. The first theoretical results have highlighted the potential of InAs based photogenerated absorbers [28]. However, a detailed study allowing us to quantify the required pump power and the impact of the carrier diffusion is still lacking.

In this work, we study the crucial impact of the photocarrier diffusion for the control of THz radiation with a metasurface. We study the modulation of the absorption coefficient for THz waves interacting with an InAs slab standing in air; see Fig. 1. The electromagnetic properties of the slab are examined for a photogenerated grating of variable pitch. This geometry is shown to support several absorption mechanisms that critically depend on the thickness of the InAs slab. For three increasing thicknesses of $0.1L_a$, $1L_a$, and $3L_a$, Fabry-Perot resonances, complex dielectric-metal or metal-metal grating absorption, and epsilon near-zero (ENZ) absorption are demonstrated [29–32]. This diversity of photonics effects is exploited to create broadband or resonant modulations that are dependent on the polarization of the THz waves. The modulation of the THz absorption is demonstrated to reach 30% to 50% for a low pump fluence of only tens of W/cm^2 when the InAs slab's thickness is varied between about 1 to 15 μm. These results are obtained with a home-made multiphysics code based on the finite element method (FEM) coupled to rigorous coupled wave analysis (RCWA) that simultaneously solves the ambipolar transport equation and the electromagnetic problems at the IR and THz frequencies [33,34]. In Sec. II, we develop a theoretical analysis for the resolution of the ambipolar transport equation in the case of a periodic pump excitation. In Sec. III, we study the electronic and electromagnetic properties of an InAs slab whose thickness h takes three increasing values of $0.1L_a$, $1L_a$, and $10L_a$. For each thickness, we track the evolution of the THz absorption peaks for both polarizations when the grating period is varied.

II. THEORY AND MODEL

We consider an undoped InAs slab of thickness h enlightened by an IR pump of wavelength $\lambda_{\mathrm{IR}} = 815$ nm corresponding to titanium-sapphire laser emission; see Fig. 1. At this wavelength, the relative permittivity of InAs is $\epsilon_{\mathrm{IR}}^{\mathrm{InAs}} = 13.64 + 3.3i$ [26]. To photogenerate grating patterns at THz frequencies, the IR pump is split into two tilted plane waves of respective incident angles $\pm\theta$ that propagate the half of the incident pump fluence denoted Φ_0. This interferential process allows us to periodically vary the electric field intensity within the InAs slab:

$$|E_{\mathrm{IR}}(x, y)|^2 = 2Z_0\Phi_0|E(y)|^2[1 + \cos(2\pi x/d)], \quad (2)$$

where $E(y)$ is a normalized total electric field calculated using the scattering matrix method [35], Z_0 is the vacuum impedance and d is the spatial period along the x direction. This grating pitch is correlated to the angle θ by the following expression: $d = \lambda_{\mathrm{IR}}/(2\sin\theta)$.

Within the InAs slab, the pump photogenerates electron-hole pairs whose density N is governed by the ambipolar transport equation [36]:

$$\frac{\partial N}{\partial t} = G^{op} - \frac{N}{\tau_r} + D_a\Delta N, \quad (3)$$

where for InAs the recombination time of the photocarriers is $\tau_r = 10^{-7}$ s and the ambipolar diffusion coefficient is $D_a = 23.5$ cm^{2}s^{-1} at room temperature (300 K) [37]. The generation term G^{op} is related to the electric field intensity by

$$G^{op}(x, y) = \pi/(hcZ_0)\,\mathrm{Im}(\varepsilon_{\mathrm{IR}})|E_{\mathrm{IR}}(x, y)|^2. \quad (4)$$

In this work, the radiative bimolecular recombination B is neglected since the pump fluence is limited in order to keep the carrier density lower than 10^{17} cm^{-3}. In these conditions, the radiative recombination BN^2 has a minor impact in contrast to the photocarrier recombination N/τ_r. For a harmonic pump excitation, the carrier density reaches a steady state and Eq.(4) becomes

$$\Delta N(x, y) - \frac{N(x, y)}{L_a^2} = -\frac{G^{op}(x, y)}{D_a}, \quad (5)$$

where the ambipolar diffusion length defined by $L_a = \sqrt{D_a\tau_r}$ is equal to 15.32 μm for InAs. Since the IR electric field intensity is a periodic function in the x direction it implies that both the source term $G^{op}(x, y)$ and the density of the photogenerated carriers are periodic functions (of period d)

that decompose in Fourier series:

$$N(x, y) = \sum_{n=-\infty}^{\infty} N_n(y) e^{inKx}, \tag{6}$$

$$G^{op}(x, y) = \sum_{n=-\infty}^{\infty} G_n^{op}(y) e^{inKx}, \tag{7}$$

where $K = 2\pi/d$ is the spatial frequency. In this framework, Eq. (5) becomes

$$\frac{\partial^2 N_n(y)}{\partial y^2} - \left((nK)^2 + \frac{1}{L_a^2}\right) N_n(y) = -\frac{G_n^{op}(y)}{D_a}. \tag{8}$$

We numerically solve the latter equation using a finite difference method which allows us to take into account the non uniform spatial distribution of the source term within the InAs slab [34]. Assuming that the surface recombinations are neglected at both interfaces, the carrier density reads

$$N(x, y) = N_0(y) + N_1(y)\cos(Kx). \tag{9}$$

These photogenerated carriers are responsible for the modification of the InAs electromagnetic properties at THz frequency. The optically induced variation of the relative permittivity is modeled with a Drude model:

$$\epsilon_{\mathrm{THz}}(x, y) = \epsilon_\infty \left(1 - \frac{\omega_p^2(N(x, y))}{\omega^2 + i\omega/\tau(N)}\right). \tag{10}$$

At THz frequencies, $\epsilon_\infty = 12.3$ for InAs semiconductor and the local plasma frequency ω_p is

$$\omega_p(x, y) = \sqrt{N(x, y)e^2/(m_{\mathrm{eff}}\epsilon_0\epsilon_\infty)}. \tag{11}$$

The local modification of $\omega_p(x, y)$ allows us to drastically change the nature of InAs: in the areas where the plasma frequency ω_p is larger than the operating THz frequency, the dielectric semiconductor transforms into a metal. In addition, the relaxation time $\tau(N) = \mu m_{\mathrm{eff}}/e$ depends on the photocarrier concentration. The mobility μ and the effective mass m_{eff} are modified by the carrier density [38]. We extract these parameters from Hall effect and reflectance measurements by the following empirical relations [39–41]

$$\mu(x, y) = \frac{2}{1 + \sqrt{0.25N(x, y)10^{-17}}} \ (\mathrm{m^2V^{-1}s^{-1}}). \tag{12}$$

$$m_{\mathrm{eff}}(x, y) = \{0.02 + 2.3[N(x, y)]^{0.335} \times 10^{-8}\}m_0, \tag{13}$$

where m_0 is the electron's mass. Using Eq. (10), the relative permittivity at THz frequencies for InAs is numerically computed and reads

$$\epsilon_{\mathrm{THz}}(x, y) = \epsilon_0(y) + \Delta\epsilon(y)\cos(Kx), \tag{14}$$

where $\epsilon_0(y)$ is the average permittivity in the x direction and $\Delta\epsilon(y)$ represents the permittivity modulation. Finally, we use a homemade RCWA code [33] to calculate the electromagnetic properties of the metasurfaces enlightened by a THz plane wave. The absorption spectra are derived from the calculation of the reflexion (R) and transmission (T) coefficients using $A = 1 - R - T$, where A is the absorption coefficient. In order to correctly simulate the complex spatial distribution of $\epsilon_{\mathrm{THz}}(x, y)$, the InAs slab is divided into a subset of layers (of thickness $L_a/5$). Armed with our multiphysics code, we analyze the electromagnetic properties of the InAs slab as a function of the pitch d, the thickness h, the pump fluence Φ_0, and the polarization of the THz wave. We restrict this study to the normal incidence for the THz plane wave.

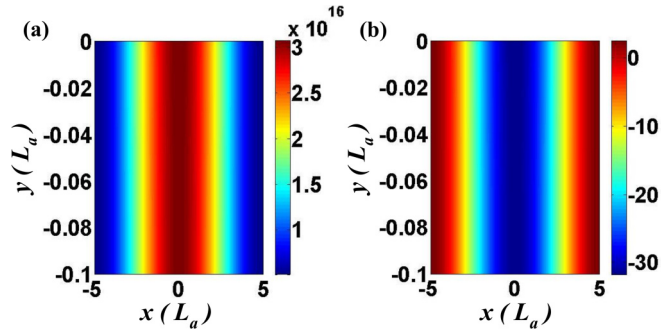

FIG. 2. Maps of the carrier density (a) and of the real part of the relative permittivity (b) for a pitch $d = 10L_a$, a thickness $h = 0.1L_a$ at $\lambda = 15L_a$, and for a pump fluence of 10 $\mathrm{W\,cm^{-2}}$.

III. STUDY

The electromagnetic properties of the photogenerated metasurfaces are studied for three thicknesses of $0.1L_a$, $1L_a$, and $3L_a$ in order to reveal the impact of the carrier diffusion within the InAs slab. The efficiency of the structures is evaluated by calculating the absorption coefficient for the THz radiation. When the pump is turned on, electromagnetic losses are introduced for the THz waves whereas when the pump is turned off the THz absorption is null since InAs is a dielectric. A modulation rate for the THz absorption of 10 MHz is expected owing the value of the InAs recombination time τ_r.

A. Thin films

We start with photogenerated gratings into a thin InAs slab of thickness $h = 1.5$ μm ($0.1L_a$), which is very small compared to the ambipolar diffusion length and to the wavelength of the THz plane wave that lies in the range of 120 to 400 μm. We first consider a low pump fluence $\Phi_0 = 10$ $\mathrm{W\,cm^{-2}}$. Figure 2 represents the photogenerated carrier density for a pitch $d = 153.2$ μm ($10L_a$) and the optically induced real part of the relative permittivity calculated at $\lambda = 229.8$ μm ($15L_a$). The maximum carrier density of 3.1×10^{16} $\mathrm{cm^{-3}}$ is reached where the electric field of the pump is maximum. We observe that the relative permittivity $\epsilon_{\mathrm{THz}}(x, y)$ only varies along the x direction with the pump modulation. In contrast, $\epsilon_{\mathrm{THz}}(x, y)$ is almost constant in the y direction since for a slab thickness smaller than the ambipolar diffusion length L_a the gradient of the carrier density in the y direction is weak. The lateral pump modulation induces nevertheless a modulation of $\epsilon_{\mathrm{THz}}(x, y)$ in the x direction that critically depends on the scale of the pitch d compared to L_a. To understand the electromagnetic response at THz frequency, we calculate the real parts of the average

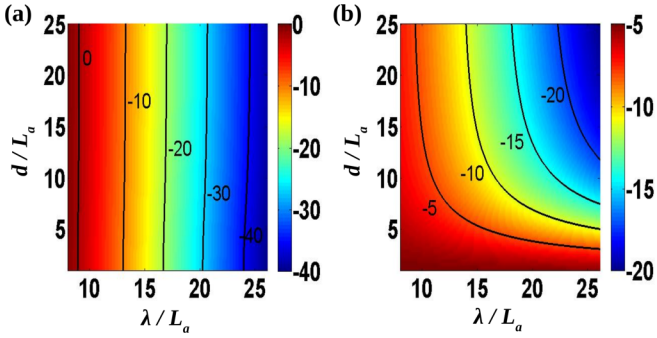

FIG. 3. (a) Average relative permittivity $\bar{\epsilon}$ and (b) permittivity variation $\Delta\bar{\epsilon}$ with respect to the normalized wavelength and the pitch d for a thin slab of $h = 0.1L_a$ and a pump fluence of 10 W cm^{-2}.

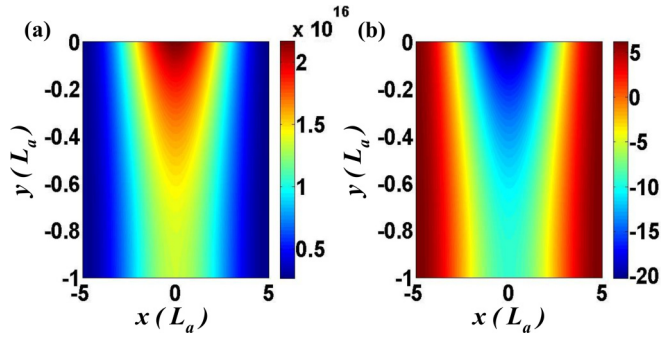

FIG. 5. Maps of the carrier density (a) and of the real part of the relative permittivity (b) for a pitch $d = 10L_a$, a thickness $h = L_a$ at $\lambda = 15L_a$, and for a pump fluence of 50 W cm^{-2}.

permittivity and the permittivity variation defined by

$$\bar{\epsilon} = \frac{1}{h}\int_0^h \epsilon_0(y)dy, \tag{15}$$

$$\Delta\bar{\epsilon} = \frac{1}{h}\int_0^h \Delta\epsilon(y)dy. \tag{16}$$

These parameters are plotted as a function of the normalized wavelength λ/L_a and the pitch d/L_a; see Fig. 3. The average permittivity map shows that the InAs slab behaves like a metallic layer for wavelengths larger than $10L_a$ regardless of the pitch of the grating [Fig. 3(a)]. In parallel, the permittivity variation $\Delta\bar{\epsilon}$ increases at large wavelengths and is sensitive to the pitch d because of the free carriers lateral diffusion [Fig. 3(b)]. When d is small enough, typically $d < 5L_a$, $\Delta\bar{\epsilon}$ decreases and saturates since the carriers diffuse between consecutive pump spots. In that case, the permittivity is almost homogeneous within the InAs slab. These results suggest that two kinds of photogenerated structures can be realized in a thin InAs layer: homogeneous metallic slabs (HS) are obtained for a pitch $d < 5L_a$ while metallic grating structures (GS) are generated when $d > 5L_a$. To verify this assertion, we plot the THz absorption spectra for several pitches; see Fig. 4. The maps of the absorption coefficient calculated with respect to the normalized wavelength and the pitch show that the THz absorption strongly depends on the polarization of the THz waves. For the TE polarization case (the electric field is perpendicular to the x-y plane), an absorption between 30% to 40% is reached for the HS ($d < 5La$) and for a broadband wavelength range spanning from $15L_a$ (225 μm) to $26L_a$ (400 μm) [Fig. 4(a)]. For the TM polarization case (the magnetic field is perpendicular to the x-y plane), the absorption coefficient attains 45% when a metallic GS is optically induced [Fig. 4(b)].

These results demonstrate that, for a weak pump fluence, a thin InAs film is equivalent to a metallic slab. An increase of the pump fluence results in realizing a metallic layer of very high negative real and imaginary parts for the permittivity. In that case, the THz waves are strongly reflected by the InAs slab which decreases its absorption. To circumvent this limitation, we consider a thicker InAs slab in order to decrease the carrier density, and to increase the electromagnetic wave interaction with the InAs slab.

B. Thick films

In this section, we study an InAs slab of thickness $h = 15.32$ μm which is equivalent to one diffusion length L_a. A pump fluence of 50 W cm^{-2} is used to maintain a sufficient carrier density. In this framework, the carrier density calculated for a pitch $d = 10L_a$ and at $\lambda = 15L_a$ presents gradual variations in both x and y directions and attains a maximal value of 2.2×10^{16} cm^{-3} [Fig. 5(a)]. This value is comparable to that observed for the thin layer but is now obtained for a pump

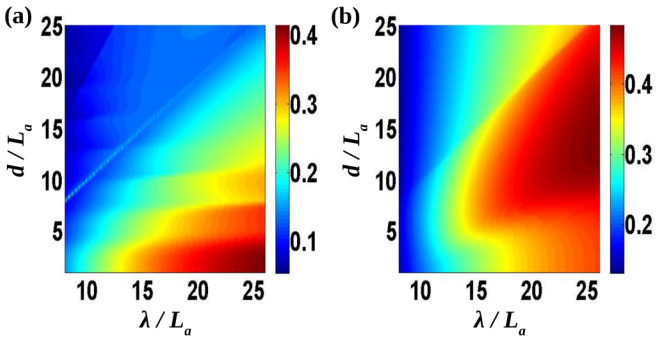

FIG. 4. Absorption spectra calculated for TE (a) and TM (b) polarization cases with respect to the normalized wavelength and pitch. The InAs thickness is $h = 0.1L_a$ and the pump fluence is 10 W cm^{-2}.

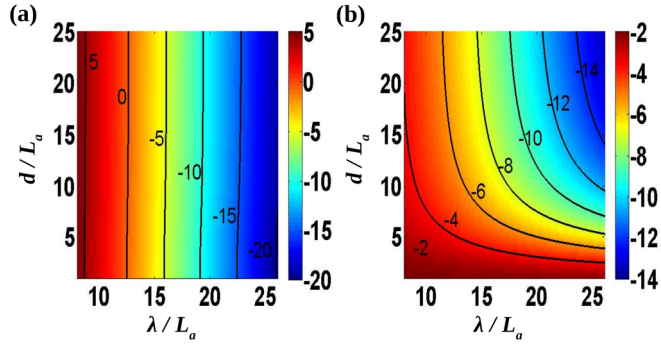

FIG. 6. (a) Average relative permittivity $\bar{\epsilon}$ and (b) permittivity variation $\Delta\bar{\epsilon}$ with respect to the normalized wavelength and the pitch d for thick thickness material $h = L_a$ and a pump fluence 50 W cm^{-2}.

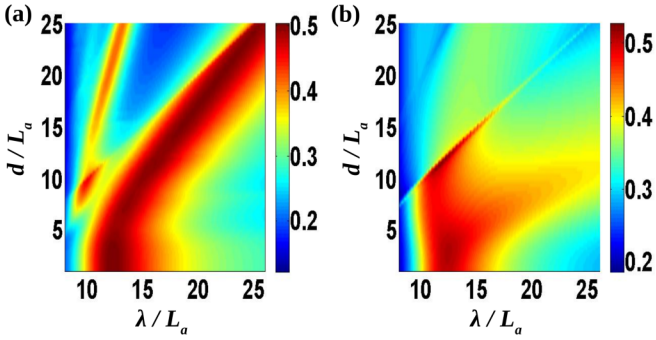

FIG. 7. Absorption spectra calculated for TE (a) and TM (b) polarization cases with respect to the normalized wavelength and the pitch. The InAs thickness is $h = L_a$ and the pump fluence is 50 W cm^{-2}.

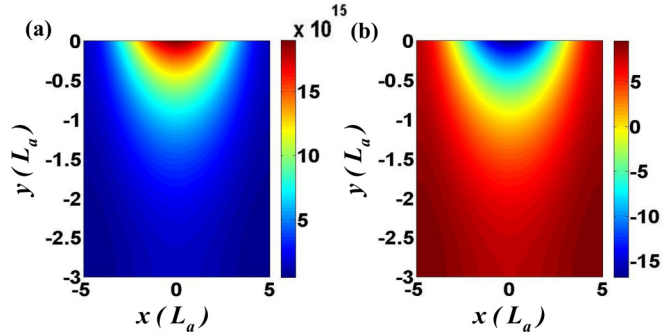

FIG. 9. Maps of the carrier density (a) and of the real part of the relative permittivity (b) for a pitch $d = 10L_a$, a thickness $h = 3L_a$ at $\lambda = 15L_a$, and for a pump fluence of 50 W cm^{-2}.

fluence five larger. When h is increased, the photocarriers are indeed able to diffuse into the InAs layer which in turn decreases their density. The photogenerated permittivity calculated at $\lambda = 15L_a$ varies in both directions and shows that the InAs layer is mostly a metal laterally sandwiched between two dielectric areas [Fig. 5(b)]. The average permittivity and its variation with respect to the wavelength and the grating pitch are plotted in Fig. 6 to identify the different kind of structures that can be photogenerated. The average permittivity is shown to vary from positive to negative values when the wavelength increases. This transition arises around $\lambda = 183.84\ \mu$m ($12L_a$), where the real part of the average permittivity is near zero: $\mathrm{Re}(\bar{\epsilon}) = 0$. The permittivity variation $\Delta\bar{\epsilon}$ shows again that the InAs slab behaves as a HS or a GS when d is either smaller or larger than $5L_a$. However, according to the wavelength, several types of HS can be optically induced ranging from lossy dielectrics, to epsilon-near-zero (ENZ) layers, to metallic layers. When $d > 5L_a$, dielectric or metallic grating structures are respectively obtained for wavelengths respectively lower or larger than $12L_a$.

This variety of structures engenders several absorption mechanisms for the THz waves which depends on their polarization; see Fig. 7. For the TE-polarization case, the grating regime (GS) in particular allows one to monitor an absorption line over a wide range of wavelengths ($12L_a$–$25L_a$) by varying the pump period d and for a constant fluence [Fig. 7(a)]. At shorter pitches, for $d < 5L_a$ when HS are photogenerated, a 50% absorption peak is reached around $\lambda = 12L_a$ for both polarizations. In this regime, a Fabry-Perot resonance traps efficiently the THz waves within an ENZ homogeneous slab which boosts the absorption. This effect occurs for a wavelength close to the average plasma wavelength denoted $\bar{\lambda_p}$ and defined by $\mathrm{Re}[\bar{\epsilon}(\bar{\lambda_p})] = 0$. It can be seen from Eq. (10) that $\bar{\lambda_p}$ is linked to the average carrier density $\bar{N_0}$, which is driven by the pump fluence. We deduce that $\bar{\lambda_p} = C/\Phi_0$, where C is a constant that depends on material parameters. This property allows one to control the spectral position of the ENZ absorption line by varying the pump fluence. For example, for $d = 2.5L_a$, the ENZ absorption peak varies from $8L_a$ to $26L_a$ with a constant efficiency of 50% when the pump fluence varies from 25 to 100 W cm^{-2}; see Fig. 8. It is worth noting that this ENZ absorption mechanism is particularly well suited to realize a broadband dynamic THz absorber. From a practical point of view it can be realized with a uniform pump since it does not stem from the spatial modulation of the permittivity. To conclude this section, InAs layers of thicknesses settled about one ambipolar diffusion length offer a wide control over the THz radiations by means

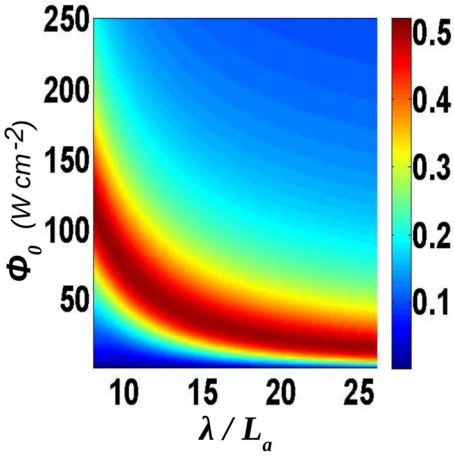

FIG. 8. Absorption spectra calculated with respect to the pump fluence and the normalized wavelength. The InAs thickness is $h = L_a$ and the pitch $d = 2.5L_a$.

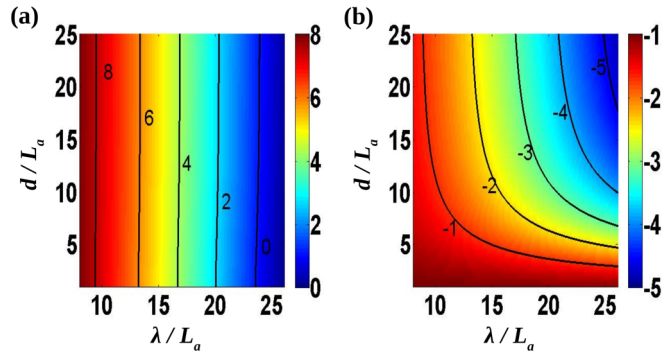

FIG. 10. (a) Average relative permittivity $\bar{\epsilon}$ and (b) permittivity variation $\Delta\bar{\epsilon}$ with respect to the normalized wavelength and the pitch d for ultrathick thickness of material $h = 3L_a$ and a pump fluence of 50 W cm^{-2}.

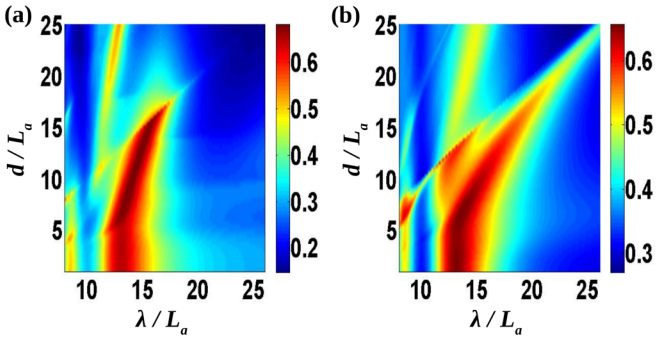

FIG. 11. Absorption spectra calculated for TE (a) and TM (b) polarization cases with respect to the normalized wavelength and the pitch. The InAs thickness is $h = 3L_a$ and the pump fluence is 50 W cm^{-2}.

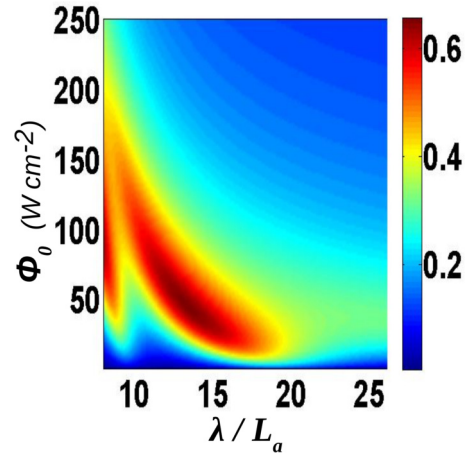

FIG. 12. Absorption spectra calculated with respect to the pump fluence and the normalized wavelength. The InAs thickness is $h = 3L_a$ and the pitch $d = 2.5L_a$.

of the modulation of the period of the optically induced grating and by the variation of the pump power.

C. Ultrathick films

Let us consider an ultrathick InAs layer whose thickness $h = 45.96\ \mu$m ($3L_a$) is larger than the ambipolar diffusion length. For a pump fluence of 50 W cm^{-2}, a pitch $d = 10L_a$, and $\lambda = 15L_a$, the carrier density presents strong gradual variations in the y-direction and reaches a maximal value about 1.9×10^{16} cm^{-3} [Fig. 9(a)]. This carrier spatial distribution generates a metallic inclusion into a dielectric host [Fig. 9(b)]. This permittivity map resembles a metallic grating whose footprint is limited to a thickness of L_a within the InAs layer. The average relative permittivity and permittivity modulation maps confirm that ultra-thick InAs layer exposed to a low pump are dielectric structures presenting a small metallic area (Fig. 10). The spectra obtained for both TE ant TM polarized THz waves show that high absorption up to 67% is reached for a small range of wavelength restricted between $13L_a$ and $15L_a$ (Fig. 11). We again remark that the same efficiency is obtained for both polarization cases when HS are formed for $d < 5L_a$. This absorption peak appears close to the average plasma wavelength derived for a $h = L_a$ thick layer. This suggest that the THz waves interact with a ENZ layer whose thickness is restricted to a distance of about L_a where the permittivity presents a noticeable modification.

To evaluate the dynamic control of the ENZ absorption which arises for unpolarized THz waves, we calculate the absorption spectra for $d = 2.5L_a$ and for a varying pump fluence (Fig. 12). The fundamental Fabry-Perot resonance appears in a small range of wavelengths between $12L_a$ and $15L_a$ when the pump fluence increases from 25 to 100 W cm^{-2}. Finally, an increase of the InAs layer thickness beyond L_a enhances the absorption of the THz wave but lowers the spectral dynamic control of the absorption lines.

IV. CONCLUSION

We have investigated photogenerated metasurfaces for realizing fast and efficient dynamic THz absorbers. Indium arsenide is demonstrated to be a promising material that tackles the actual limitations of this approach. The diffusion of the photocarriers plays a crucial role for realizing grating or homogeneous structures when a spatially modulated pump is considered. The study of the electronic and electromagnetic properties of an InAs layer shows that resonant absorption lines are monitored by the pump fluence and by the spatial period of the pump. These properties drastically depend on the InAs layer thickness compared to the ambipolar diffusion distance. For a 45 μm thick InAs layer, the modulation of the THz absorption coefficient is demonstrated to increase with the thickness and attains 67% for a CW pump power of only 50 W cm^{-2}. In contrast, thin layers of about 1.5 μm present an absorption of 40% for a very low fluence of 10 W cm^{-2}. However, the best dynamical control for monitoring the absorption lines is obtained for a thickness of 15 μm, which corresponds to an ambipolar distance. In that case, a Fabry-Perot resonance arises close to ENZ regime and boosts the absorption to 50%. This ENZ absorption can be optically actuated over a broad frequency band ranging from 1 to 3 THz when the pump fluence is increased from 25 to 100 W cm^{-2}. These results open promising avenues for realizing on-chip active THz components based on InAs, since low pump powers of only 500 mW can be easily delivered by integrated CW lasers. All the authors provided technical and scientific insight and contributed to the writing of the manuscript.

[1] S. S. Dhillon, M. S. Vitiello, E. H. Linfield, A. G. Davies, M. C. Hoffmann, J. Booske, C. Paoloni, M. Gensch, P. Weightman, G. P. Williams *et al.*, J. Phys. D: Appl. Phys. **50**, 043001 (2017).

[2] J. F. Federici, B. Schulkin, F. Huang, D. Gary, R. Barat, F. Oliveira, and D. Zimdars, Semicond. Sci. Technol. **20**, S266 (2005).

[3] K. I. Zaitsev, N. V. Chernomyrdin, K. G. Kudrin, I. V. Reshetov, and S. O. Yurchenko, J. Phys. Conf. Ser. **584**, 012023 (2015).

[4] S. Koenig, D. Lopez-Diaz, J. Antes, F. Boes, R. Henneberger, A. Leuther, A. Tessmann, R. Schmogrow, D. Hillerkuss, R. Palmer, T. Zwick, C. Koos, W. Freude, O. Ambacher, J. Leuthold, and I. Kallfass, Nat. Photonics **7**, 977 (2013).

[5] N. K. Grady, J. E. Heyes, D. R. Chowdhury, Y. Zeng, M. T. Reiten, A. K. Azad, A. J. Taylor, D. A. R. Dalvit, and H.-T. Chen, Science **340**, 1340 (2013).

[6] R.-H. Fan, Y. Zhou, X.-P. Ren, R.-W. Peng, S.-C. Jiang, D.-H. Xu, X. Xiong, X.-R. Huang, and M. Wang, Adv. Mater. **27**, 1201 (2014).

[7] N. Yu, P. Genevet, M. A. Kats, F. Aieta, J.-P. Tetienne, F. Capasso, and Z. Gaburro, Science. **344**, 333 (2011).

[8] N. Yu and F. Capasso, Nat. Mater. **13**, 139 (2014).

[9] N. Yu and F. Capasso, J. Lightwave Technol. **33**, 2344 (2015).

[10] P. P. Iyer, N. A. Butakov, and J. A. Schuller, ACS Photonics **2**, 10771084 (2015).

[11] Ho-Seok Ee and R. Agarwal, Nano Lett. **16**, 2818 (2016).

[12] K. Fan and W. J. Padilla, Mater. Today. **18**, 39 (2015).

[13] W. Cai and V. Shalaev, *Optical Metamaterials: Fundamentals and Applications* (Springer, Dordrecht, 2010).

[14] T. Lewi, P. P. Iyer, N. A. Butakov, A. A. Mikhailovsky, and J. A. Schuller, Nano Lett. **15**, 81888193 (2015).

[15] I. Chatzakis, P. Tassin, L. Luo, N.-H. Shen, L. Zhang, J. Wang, T. Koschny, and C. M. Soukoulis, Appl. Phys. Lett. **103**, 043101 (2013).

[16] M. M. Shcherbakov, S. Liu, V. V. Zubyuk, A. Vaskin, P. P. Vabishchevich, G. Keeler, T. Pertsch, T. V. Dolgova, I. Staude, I. Brener, and A. A. Fedyanin, Nat. Commun. **8**, 17 (2017).

[17] T. Okada and K. Tanaka, Sci. Rep. **1**, 121 (2011).

[18] G. Georgiou, H. K. Tyagi, P. Mulder, G. J. Bauhuis, J. J. Schermer, and J. Gómez Rivas, Sci. Rep. **4**, 3584 (2014).

[19] F. P. Mezzapesa, L. L. Columbo, C. Rizza, M. Brambilla, A. Ciattoni, M. Dabbicco, M. S. Vitiello, and G. Scamarcio, Sci. Rep. **5**, 16207 (2015).

[20] G. Georgiou, C. Tserkezis, M. C. Schaafsma, J. Aizpurua, and J. Gómez Rivas, Phys. Rev. B. **91**, 125443 (2015).

[21] T. P. Steinbusch, H. K. Tyagi, M. C. Schaafsma, G. Georgiou, and J. Gómez Rivas, Opt. Express **22**, 26559 (2014).

[22] X. Wang, Z. Xie, W. Sun, S. Feng, Y. Cui, J. Ye, and Y. Zhang, Opt. Lett. **38**, 4731 (2013).

[23] C. Rizza, A. Ciattoni, F. De Paulis, E. Palange, A. Orlandi, L. Columbo, and F. Prati, J. Phys. D: Appl. Phys. **48**, 135103 (2015).

[24] C. Rizza, A. Ciattoni, L. Columbo, M. Brambilla, and F. Prati, Opt. Lett. **38**, 1307 (2013).

[25] Y. Yang, N. Kamaraju, S. Campione, S. Liu, J. L. Reno, M. B. Sinclair, R. P. Prasankumar, and I. Brener, ACS Photonics **4**, 15 (2017).

[26] E. D. Palik and R. T. Holm, *Handbook of Optical Constants of Solids* (Academic, San Diego, 1998), p. 479.

[27] C. Rizza, L. Columbo, M. Brambilla, F. Prati, and A. Ciattoni, Phys. Rev. B. **93**, 241305(R) (2016).

[28] R. Smaali, T. Taliercio, and E. Centeno, Opt. Lett. **41**, 16 (2016).

[29] J. Yoon, M. Zhou, Md. A. Badsha, T. Y. Kim, Y. C. Jun, and C. K. Hwangbo, Sci. Rep. **5**, 12788 (2015).

[30] S. Vassant, A. Archambault, F. Marquier, F. Pardo, U. Gennser, A. Cavanna, J. L. Pelouard, and J. J. Greffet, Phys. Rev. Lett. **109**, 237401 (2012).

[31] Y. C. Jun J. Reno, T. Ribaudo, E. A. Shaner, J.-J. Greffet, S. Vassant, F. Marquier, M. B. Sinclair, and I. Brener, Nano Lett. **13**, 5391 (2013).

[32] I. Liberal and E. Engheta, Nat. Photonics **11**, 149 (2017).

[33] G. Granet and B. Guizal, J. Opt. Soc. Am. **13**, 5 (1996).

[34] J. Chaskalovic, *Finite Elements Methods for Engineering Sciences* (Springer-Verlag, Berlin, 2008).

[35] J. Defrance, C. Lemaître, R. Ajib, J. Benedicto, E. Mallet, R. Pollès, J.-P. Plumey, M. Mihailovic, E. Centeno, C. Ciracì, D. Smith, and A. Moreau, J. Open Res. Softw. **4**, e13 (2016).

[36] D. A. Neamen, *Semiconductor Physics and Devices*, 4th ed. (Academic, New York, 2012)

[37] E. Rosencher and B. Vinter, *Optoelectronics* (Cambridge University Press, Cambridge, 2002).

[38] C. Rizza, A. Ciattoni, E. Spinozzi, and L. Columbo, Opt. Lett. **37**, 3345 (2012).

[39] C. Hilsum, Electron. Lett. **10**, 259 (1974).

[40] M. Levinshtein, S. Rumyantsev, and M. Shur, *Handbook Series on Semiconductor Parameters*, Vol. I (World Scientific, Singapore, 1996).

[41] H. Mathieu, and H. Fanet, *Physique Des Semiconducteurs Et Des Composants Électroniques*, 6th ed., Sciences Sup, Dunod (Dunod, 2009).